Intercomparison of the KOPRA and the RFM radiative transfer codes

N. Glatthor, M. Höpfner, G.P. Stiller,
T. von Clarmann, A. Dudhia, G. Echle,
B. Funke, and F. Hase

Abstract: We discuss the intercomparison between the Karlsruhe Optimized and Precise Radiative transfer Algorithm (KOPRA) and the Reference Forward Model (RFM) codes. The purpose of this intercomparison is to validate the KOPRA algorithm, i.e. to identify and to remove possible errors in the KOPRA (or RFM) code and to quantify the reason of remaining differences. A similar comparison between the MIPAS Optimized Forward Model (OFM) and the RFM has already been performed (Ref. [1]). To be able to relate on these results, the KOPRA validation is similarly organized: We also perform subsequently more complex tests of ray-tracing, integrated column amounts, homogeneous and limb path calculations of unapodized, apodized and field-of-view (FOV) convolved spectra, using the same isolated CO_2 line as well as the same six MIPAS microwindows. Additionally we compare the modeling of CO_2 line-mixing, non-local thermodynamic equilibrium (NLTE), trace gas continua, cross-section spectra and of derivatives of the spectra with respect to atmospheric parameters.

The KOPRA-RFM residuals are below a quarter of the noise-equivalent spectral radiance (NESR) for the isolated CO_2 line as well as for the MIPAS microwindows, i.e. KOPRA fulfills the acceptance criteria requested for the OFM. In most cases the deviations are even clearly below 1 $\mathrm{nW/(cm^2\ sr\ cm^{-1})}$, i.e. more than one order of magnitude below the acceptance threshold. This is valid for unconvolved as well as for ALS (apodized line shape) and FOV convolved spectra. There is also good agreement in modeling of the H_2O-, O_2- and N_2-continua and of CO_2 line-mixing. Larger deviations of up to several $\mathrm{nW/(cm^2\ sr\ cm^{-1})}$ were found for NLTE calculations on the basis of the "default" atmospheric profiles with vertical resolution of 1 or 2.5 km. These differences were found to be due to different layer-averaging of the vibrational temperatures and could be considerably reduced by calculations with a higher vertical resolution of 250 m. Cross-section spectra agree well, if the tabulated data are given independent of pressure, e.g. for $ClONO_2$ and N_2O_5, and cover the atmospheric temperatures. Due to different temperature extrapolation the deviations increase up to 10 $\mathrm{nW/(cm^2\ sr\ cm^{-1})}$ for atmospheric temperatures outside the tabulated range. The RFM is not yet adjusted to cross-sections given for non-equidistant temperatures and for atmospheric pressures, like CFC data in the HITRAN96 database. If these data are used, larger differences arise, e.g. up to 30 $\mathrm{nW/(cm^2\ sr\ cm^{-1})}$ between CFC-12 spectra. Avoidance of interpolation by performing homogeneous path calculations for p, T of one of the tabulated cross-section datasets reduces the deviations to below 0.5 $\mathrm{nW/(cm^2\ sr\ cm^{-1})}$.

1 Introduction

The Karlsruhe Optimized and Precise Radiative transfer Algorithm (KOPRA) has been developed for data analysis of the Michelson Interferometer for Passive Atmospheric Sounding (MIPAS), which will be launched on the polar-orbiting Environmental Satellite 1 (ENVISAT-1). KOPRA is a line-by-line model of high numerical accuracy, which (as far as foreseeable) can handle all atmospheric and instrumental effects necessary for the modeling of the MIPAS spectra, e.g. ray-tracing for an ellipsoidal earth shape including refraction, horizontal atmospheric inhomogeneities, NLTE conditions, CO_2 line-mixing, cross-sections to model the spectra of heavy molecules (CFCs, $ClONO_2$, N_2O_5), varying abundances of isotopomeres, parameterization of the instrumental line shape (ILS), and modeling of the instrumental FOV with regard to refraction.

KOPRA has a flexible structure enabling fast calculations for routine operation but also dedicated scientific studies. Most of the special effects just mentioned can be switched on or off, and the required accuracy for the calculation of the optical depth, for the layering of the atmosphere, for the apodization function and for other

parameters influencing computational speed can be varied by the user. Whereas KOPRA's default accuracy for the calculation of the optical depth is 10^{-5}, the spectra presented here were generally calculated with an accuracy of 10^{-10}. But we will exemplarily show the convergence of the KOPRA spectra towards the RFM results for increasing accuracy. A more detailed description of KOPRA's concept is given in Ref. [2].
The MIPAS Reference Forward Model (RFM) has been derived from GENLN2 to generate "true" reference spectra for validation of the operational codes for the analysis of the MIPAS data (Ref. [3]). Therefore the RFM is designed to perform calculations with high accuracy rather than computational speed.
In this document we compare KOPRA Version 0.4 with RFM Version 3.0 (Version 3.6 for NLTE calculations), which were supplied by the University of Oxford. For readers interested in a more compact presentation of the intercomparison we refer to Ref. [4].

2 Intercomparison Set-Up

2.1 Acceptance Criteria

The forward model errors should be significantly below the uncertainty of the MIPAS experiment and of the retrieval error. We set an acceptance threshold of 25% of noise-equivalent spectral radiance (NESR) for differences between KOPRA and RFM spectra, i.e. approximately
12.5 nW/(cm^2 sr cm^{-1}) in channel A (685 - 970 cm^{-1}),
5 nW/(cm^2 sr cm^{-1}) in channel B (1215 - 1500 cm^{-1}).
1 nW/(cm^2 sr cm^{-1}) in channel D (1820 - 2410 cm^{-1}).

2.2 Data Bases and Assumptions

Generally we use the same databases and make the same assumptions as in the OFM-RFM intercomparison.

Atmosphere

FASCODE 'model6' atmosphere (1976 US Standard); additionally a midlatitude HNO_3 profile of a climatology (Ref. [5]). For LTE calculations the original atmospheric profiles with 50 levels between 0 and 120 km were used, i.e. 1 km vertical spacing up to 25 km, 2.5 km spacing between 25 km and 50 km and 5 km spacing above 50 km. NLTE modeling of CO_2 was performed using profiles with 1 km and 250 m vertical sampling. NLTE-spectra of NO were calculated for an atmosphere extending up to 200 km and 2.5 and 250 m height resolution. For the RFM the Earth's radius of curvature at the tangent point was set to 6367.421 km, whereas KOPRA calculations were performed for an ellipsoidal Earth with a major axis of 6378.137 km, a minor axis of 6356.752 km (WGS84) and southward observation with tangent point at 45oN. To be able to compare both codes using the same limb geometry, a "downgraded" KOPRA-version calculating with a spherical Earth of radius 6367.421 km was additionally created.

Line Data

Line data were taken from the HITRAN96 line data base (Ref. [6]) and total internal partition sums (TIPS) were calculated according to the HITRAN96 TIPS code. For HNO_3, updated TIPS provided by Gamache were used for both codes (Gamache, pers. commun., 1997).

Table 1: CO_2 column amounts U calculated by KOPRA and RFM for different homogeneous atmospheres, path length = 250 km, CO_2 *vmr* = 330 ppmv.

Press. [hPa]	Temp. [K]	U_{KOPRA} [kmole/cm^2]	U_{RFM} [kmole/cm^2]
250.000	220	1.12755×10^{-4}	1.12755×10^{-4}
2.50000	250	9.92241×10^{-7}	9.92241×10^{-7}
0.20000	240	8.26868×10^{-8}	8.26868×10^{-8}
0.01000	200	4.96121×10^{-9}	4.96121×10^{-9}
0.00004	300	1.32299×10^{-11}	1.32299×10^{-11}

Table 2: Path lengths S through the 1976 US Standard Atmosphere calculated by KOPRA and RFM for different tangent heights and spherical Earth, refraction included.

Tght. [km]	S_{KOPRA} [km]	S_{RFM} [km]	Diff. [km]
10	1208.977	1208.975	0.002
20	1139.060	1139.063	-0.003
40	1015.850	1015.850	0.000
60	880.291	880.291	0.000
80	719.302	719.302	0.000

Line Shape

Apodization was performed in spectral space with the Norton-Beer no. 3 (strong) function (Ref. [7]); instrumental self-apodization and other line shape distortions were not considered.

Field-of-View

The FOV was modeled by the trapezoidal vertical response function defined by ESA, which is constant up to ±1.4 km apart from the tangent point and then decreases linearly to zero at ±2.0 km distance.

Interpolation

Both KOPRA and the RFM linearly interpolate log pressure ($\ln p$), temperature T and volume mixing ratio *vmr* between profile levels.

Wavenumber Grids

Two different wavenumber grids were used:

(a) a fine grid with 0.0005 cm^{-1} spacing for unapodized spectra and

(b) a coarse grid with 0.025 cm^{-1} spacing for apodized spectra.

The fine grid is commonly used for middle-atmosphere modeling (Doppler broadening typically $>$ 0.001 cm^{-1}). The coarse grid will be the standard format for the representation of apodized MIPAS spectra.

Table 3: CO_2 column amounts U calculated by KOPRA and RFM for different limb paths through the 1976 US Standard Atmosphere and spherical Earth, refraction included.

Tght. [km]	U_{KOPRA} [kmole/cm^2]	U_{RFM} [kmole/cm^2]	Diff. %
10	1.26011×10^{-4}	1.26011×10^{-4}	0.000
20	2.57658×10^{-5}	2.57661×10^{-5}	-0.001
40	1.23681×10^{-6}	1.23689×10^{-6}	-0.006
60	9.67691×10^{-8}	9.67899×10^{-8}	-0.021
80	5.03587×10^{-9}	5.03652×10^{-9}	-0.013

Table 4: Curtis-Godson pressures calculated by KOPRA and RFM for several segments of a 10 km tangent-height path for N_2O (1976 US Standard Atmosphere). Calculations of both codes for spherical Earth.

Segment [km]	$\bar{p}_{g,KOPRA}$ [hPa]	$\bar{p}_{g,RFM}$ [hPa]	Rel. Diff.
10-11	$2.524114\times10^{+2}$	$2.524111\times10^{+2}$	1.19×10^{-6}
20-21	$5.137634\times10^{+1}$	$5.137519\times10^{+1}$	2.24×10^{-5}
40-42.5	$2.502353\times10^{+0}$	$2.502152\times10^{+0}$	8.03×10^{-5}
95-100	5.482884×10^{-4}	5.481659×10^{-4}	2.23×10^{-4}

Table 5: Curtis-Godson temperatures calculated by KOPRA and RFM for several segments of a 10 km tangent-height path for N_2O (1976 US Standard Atmosphere). Calculations of both codes for spherical Earth.

Segment [km]	$\bar{T}_{g,KOPRA}$ [K]	$\bar{T}_{g,RFM}$ [K]	Diff.
10-11	221.2131	221.2130	0.0001
20-21	217.1286	217.1287	-0.0001
40-42.5	253.3470	253.3484	-0.0014
95-100	191.1491	191.1504	-0.0013

3 Path Lengths and Integrated Column Amounts

First we compared integrated column amounts for homogeneous paths and then the ray-tracing algorithms for limb-paths, i.e. path lengths, integrated column amounts and Curtis-Godson pressures and temperatures. The integrated column amount U_g (kmoles/cm^2) is the primary path integral

$$U_g = \int_{path} \rho_g ds, \tag{1}$$

whereby ρ_g is the molar absorber density (kmoles/cm^3) of gas g and ds the path element. Both KOPRA and the RFM approximate inhomogeneous limb-paths by a number of segments, each having constant absorber amount u_g (kmoles/cm^2), pressure and temperature:

$$u_g = \int_{seg} \rho_g ds, \tag{2}$$

$$\bar{p}_g = \frac{1}{u_g} \int_{seg} p \rho_g ds, \tag{3}$$

$$\bar{T}_g = \frac{1}{u_g} \int_{seg} T \rho_g ds. \tag{4}$$

The weighted quantities $\bar{p}_g$ and $\bar{T}_g$ are the Curtis-Godson pressure and temperature of gas g.

Table 1 shows CO_2 column amounts calculated for homogeneous paths through 5 different atmospheres with constant *p, T* and *vmr* (cuvette calculations). In the frame of the representation there is no difference between the KOPRA and RFM results.

To have the same limb geometry for both codes, a "downgraded" KOPRA version calculating with a spherical Earth of radius 6367.421 km was created (change in module param_m.f90). In KOPRA, ray-tracing is performed by calculating the differential displacement of the ray path (Ref. [8]), whereas the RFM uses Snell's law applied to a sphere (Ref. [3]). However, the path lengths through the 1976 US Standard Atmosphere, considering refraction, are in very good agreement (Table 2). For tangent altitudes of 40 km and above they differ by less than 1 m, towards lower altitudes they slightly increase to -3 m at 20 km and to 2 m at 10 km.

The difference between integrated CO_2 column amounts is less than 0.001% for 10 km tangent height and increases to -0.02% at 60 km altitude (Table 3). Similar deviations were found in the OFM-RFM intercomparison. The differences between Curtis-Godson pressures for a 10 km tangent-height path for N_2O increase from 0.0001% for the lowermost segment to 0.02% for the segment from 90 to 95 km (Table 4). The differences between the respective Curtis-Godson temperatures remain below 2×10^{-3} K for each segment (Table 5). We conclude that the differences in path-lengths, column amounts and Curtis-Godson parameters are negligible.

4 Spectral Calculations for Homogeneous Paths

To compare the line shapes unaffected by differences resulting from ray-tracing, we start with homogeneous paths.

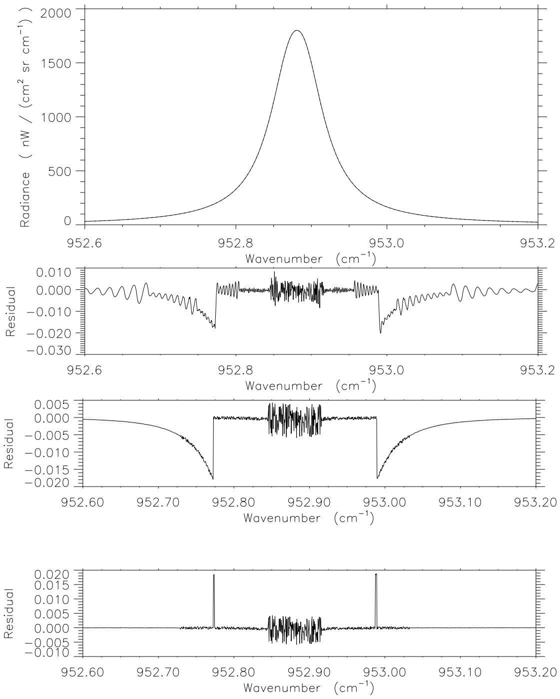

Figure 1: Unapodized radiance spectra of an isolated CO_2 line for homogeneous path conditions of 250 hPa and 220 K (top). KOPRA-RFM differences (in the same units as the radiance spectra) for calculations including χ-factor for KOPRA accuracy of 10^{-5} (second) and 10^{-10} (third) and for calculations without χ-factor (bottom) for KOPRA accuracy of 10^{-10}. The two steps at the wings of the first and second residual and the two spikes in the bottom residual are due to different Humlicek algorithm realizations.

4.1 Voigt Line Shape

Atmospheric lines are generally well described by the Voigt line shape, which is a convolution of the Lorentz and Doppler line shape functions. Both codes evaluate the Voigt line shape either by the original Humlicek algorithm (Ref. [9]), whose accuracy is 10^{-4}, or by modified versions for faster calculations (Ref. [10, 11]). The Humlicek algorithm has four evaluation regions and switches to Doppler line shape near line center and to Lorentzian line shape at the line wings.

Tests of line shape modeling were performed for the same isolated CO_2 line at 952.880858 cm^{-1} and for the same three different regimes as in Ref. [1]:

(a) Lorentz: p=250 hPa, T=220 K (~atmospheric conditions at 10 km altitude),
(b) Mixed: p=2.5 hPa, T=250 K (~40 km altitude),
(c) Doppler: p=0.2 hPa, T=240 K (~60 km altitude).

For each case a CO_2 *vmr* of 330 ppmv (1976 US value) and a pathlength of 250 km (approximately the length of a limb path through a 5 km layer above the tangent point) were assumed. Generally, CO_2-spectra were calculated including χ-factor (cf. Section 6.1), which by default is taken into account for CO_2-line modeling by KOPRA. For RFM calculations the χ-factor can be switched on or off by an external flag. Therefore a modified KOPRA-version was created (change in module abco_m.f90) to compare spectra modeled without χ-factor for the Lorentzian case. Figure 1 shows the resulting KOPRA and RFM spectra[1] (top) and the residual

---

[1] The deviations between KOPRA and RFM presented here are only visible in the difference

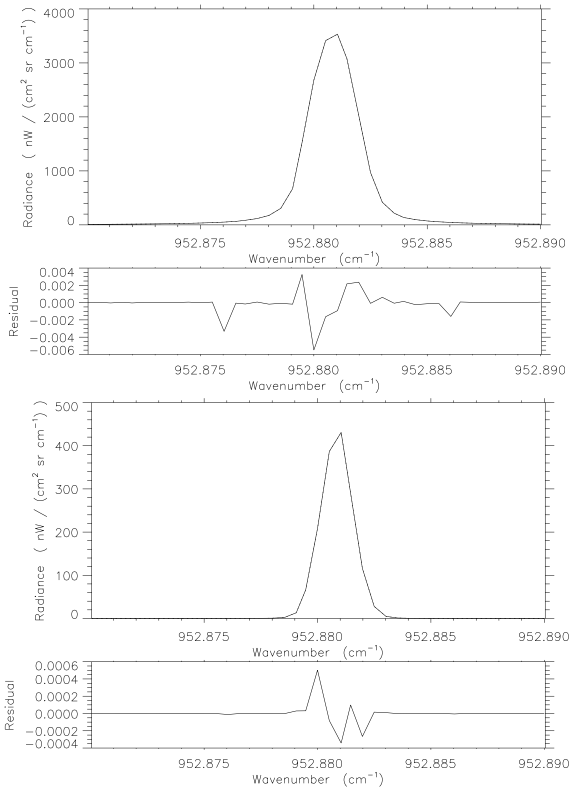

Figure 2: Unapodized radiance spectra and KOPRA-RFM differences for an isolated CO_2 line for homogeneous path conditions of 2.5 hPa and 250 K (top) and of 0.2 hPa and 240 K (bottom). KOPRA calculations of the optical depth with an accuracy of 10^{-10}.

spectra for the Lorentzian case including (second, third) and without χ-factor (bottom), whereby KOPRA's accuracy for the calculation of the optical depth was 10^{-5}, 10^{-10} and 10^{-10}, respectively. The weak oscillations in the case of default accuracy (10^{-5}) are due to quadratic interpolation of the absorption coefficients on the fine grid by KOPRA. In the case of high accuracy KOPRA calculates all absorption coefficients explicitely and the oscillations disappear. The steps of -0.02 nW/(cm^2 sr cm^{-1}) at the wings of the first two residual spectra are due to discontinuities between the different evaluation regions of the fast Humlicek algorithm which was applied by KOPRA to calculate the Voigt profile. When the CO_2 χ-factor is included, the RFM takes the standard Humlicek algorithm, which does not produce these features. However, for default calculations without χ-factor the RFM also uses the fast Humlicek algorithm, which results in a nearly complete compensation of the discontinuities in the lowermost residual. The remaining spikes of 0.02 nW/(cm^2 sr cm^{-1}) are caused by slightly different extensions of the evaluation regions (see also Appendix A). However, the magnitude of the discontinuities remains below 10^{-4}, which is anyway the accuracy limitation of the Humlicek approximation. At the line center, the KOPRA-RFM differences are less than 0.005 nW/(cm^2 sr cm^{-1}) or less than 0.001%.

For the mixed and Doppler cases (Figure 2) the agreement with the RFM is very

---

spectra.

good, with residuals of less than 0.006 nW/(cm^2 sr cm^{-1}) and less than 0.0006 nW/(cm^2 sr cm^{-1}) at the line center, respectively. The spectral region shown is more confined to the line center than in Figure 1 and does not contain the discontinuities, because the radiances at these locations have nearly decreased to zero. E.g. for the mixed case the radiance at 953 cm^{-1} is below 0.1 nW/(cm^2 sr cm^{-1}) and the step is below 10^{-5} nW/(cm^2 sr cm^{-1}), which again means a relative discontinuity of 10^{-4}.

We conclude that for the Lorentzian case, apart from the steps at the line wings, the errors caused by the line shape approximations of KOPRA are below 0.1% of the acceptance threshold. The discontinuities are below 0.2% of NESR/4. For the mixed case the absolute uncertainties are of the same order, and for the Doppler case even lower by one order of magnitude.

4.2 Line Wing Assumptions

For spectral calculations the RFM covers the microwindow and the surrounding region by a wide-mesh of width 1 cm^{-1} (at integer wavenumbers). Inside the microwindow fine grid calculations are performed for lines centered in the respective and the two neighboring 1 cm^{-1} intervals. The absorption of further remote lines is only calculated at the edges and the centers of the wide-mesh intervals, added up and interpolated to the fine grid. KOPRA has a variable spacing for each line considered with respect to the required accuracy (Ref. [12]). The contributions of the lines are added up and interpolated quadratically to the next finer grid.

Both codes include line wing contributions of lines located in a user-defined region around the microwindow (default value ±25 cm^{-1}). For KOPRA calculations the extension region is related to the microwindow's edges and therefore the same for each line inside the microwindow. This area is further enlarged by the width of the apodization function (cf. Section 5.1.2). The RFM's extension region is applied to each edge of the 1 cm^{-1} intervals. Thus, the concepts are a little different, but approach for small microwindows and low accuracy apodization functions. Both codes can model the contribution of even further remote H_2O, CO_2, N_2 and O_2 lines by pressure and temperature dependent continua.

Line wing modeling for different microwindow extensions was compared for a H_2O-microwindow from 1413.9 to 1416.4 cm^{-1} (cf. Ref. [1]). This microwindow is influenced by the wings of strong H_2O lines just outside the window boundaries. The following atmospheric conditions were chosen: Homogeneous path of 250 km length, $p = 250$ hPa, $T = 220$ K and H_2O $vmr = 10$ ppmv. Five tests are presented:

(a) Using only lines centered inside the microwindow,

(b) Using lines within ±32 cm^{-1} from the microwindow's edges for KOPRA and ±25 cm^{-1} for RFM,

(c) Using lines within ±25 cm^{-1} from the microwindow's edges for both programs,

(d) Same as (c), but area of fine-mesh calculations of the RFM extended to ±5 cm^{-1}.

(e) Same as (c), but additionally H_2O continuum, i.e. contribution of line wings beyond ±25 cm^{-1}, taken into account.

The results of the tests are shown in Figure 3. The spectra of the cases (c) and (d) are not plotted, since they are nearly identical with those of case (b). For better interpolation of Lorentzian line wing contributions of strong H_2O lines outside the microwindow the RFM was run with the inverse quadratic (IQD) option (cf. Ref. [1]). When only lines from inside the microwindow are taken into account (a), the agreement is very good with differences generally smaller than 0.002 nW/(cm^2 sr cm^{-1}). The two spikes of 0.006 nW/(cm^2 sr cm^{-1}) and the smaller spikes at 1414.7 and 1415.2 cm^{-1} are caused by discontinuities in the fast Humlicek algorithms (cf. Section 4.1), which are slightly closer to the line center in the RFM code. For case (b) there is an offset of 0.25 nW/(cm^2 sr cm^{-1}), because KOPRA adds up line wing contributions of a larger spectral region. At the line centers the offset decreases or disappears due to saturation. This case shows that one has to keep in mind the differences in microwindow extension, when comparing KOPRA and RFM spectra. For exactly the same extension (c) the differences become much smaller. They oscillate around zero with an amplitude of 0.02 nW/(cm^2 sr cm^{-1}) and increase slightly to ±0.05 nW/(cm^2 sr cm^{-1}) at the microwindow's edges. The disappearance of these oscillations at 1414.0, 1414.5 and 1415.0 cm^{-1} and for RFM calculations with an extended fine-mesh area of ±5 cm^{-1} (d) shows, that they are caused by the line wing interpolation of the RFM (see also Appendix A). For case (e) the residuals are nearly the same as for case (c), which means that inclusion of the H_2O continuum causes no additional problems.

5 Spectral Calculations for Limb Paths

Now we compare spectral calculations for atmospheric limb-paths through the 1976 US Standard Atmosphere.

5.1 Isolated CO_2 Line, 10 km Tangent Height

5.1.1 Unconvolved Spectra

For unconvolved spectra the differences are 1-2 orders of magnitude less than NESR/4 (Figure 4). The residuals of 0.35 nW/(cm^2 sr cm^{-1}) at the line center in Figures 4b and 4c are mainly caused by the different Earth shapes assumed, which has the strongest effect at high altitudes far away from the tangent point. Non-standard KOPRA calculations for a spherical Earth reduce the spike to -0.1 nW/(cm^2 sr cm^{-1}) (Figure 4d); the remaining residual is due to slightly different Curtis-Godson temperatures. The weak oscillations in the case of KOPRA calculations with default accuracy (Figure 4b) disappear for higher accuracy (Figures 4c,d). The discontinuities at the line wings are due to different realizations of the Humlicek algorithm (cf. Section 4.1).

5.1.2 ALS Convolution

In this paper the ILS of MIPAS was assumed to be a sinc function (no self-apodization and phase errors). To simulate the apodization of the interferograms measured by MIPAS, the CO_2 line was convolved with the Norton-Beer no. 3 (strong) apodization function. KOPRA can calculate several apodization functions internally or read an external line shape function defined by the user. According to the accuracy chosen, the spectral extension of the strong Norton-Beer apodization function for 20 cm optical path difference is ±0.0755 cm^{-1}, ±0.7005 cm^{-1} or ±7.0005 cm^{-1}, respectively. The apodization function of the RFM is always supplied externally.

KOPRA normalizes the apodization function to its area up to infinity. It does not renormalize the truncated apodization function, which covers slightly less than unit area, because this concept leads to true trace gas column amounts for the retrieval of well resolved lines. The RFM renormalizes the apodization function, which is more adequate for continuum-like signatures. This results in slightly stronger apodized spectral lines, but the differences are small. For example, KOPRA's medium accuracy apodization function covers more than 99.96% of unit area.

To provide exactly the same apodization function for both KOPRA and RFM calculations, the medium accuracy strong Norton-Beer function of KOPRA was truncated to 2001 values (default RFM limitation) and renormalized to unit area

(ils2001.nor). To show the influence of different spectral extension and normalization of the apodization functions, we also present KOPRA spectra convolved with the medium accuracy function, consisting of 2801 spectral points, and with the not renormalized version of the truncated function (ils2001.abs).
Figure 5 shows the results of the ALS convolution. The medium accuracy function, which has a larger spectral extension than the RFM's function, produces a residual of -1.5 nW/(cm^2 sr cm^{-1} at the line center (Figure 5b). For KOPRA calculations with ils2001.abs, which covers slightly less than unit area, the differences are reduced by 50% (Figure 5c). Application of the renormalized apodization function ils2001.nor leads to residuals below 0.03 nW/(cm^2 sr cm^{-1}), i.e. far below 0.1% of NESR/4.

5.1.3 ALS and FOV Convolution

In the case of a vertically extended FOV the spectrum also contains contributions from below and above nominal tangent height, where different atmospheric conditions exist. KOPRA and the RFM model this effect by calculating point-radiance spectra inside and around the vertical FOV (more than 20 possible) and adding up these spectra, weighted by a FOV function. The shape of KOPRA's weighting function can be defined on 20 horizontal strips, the RFM's weighting function at up to 21 vertical grid points.
The RFM-version used for this comparison makes two simplifications in FOV modeling: (a) The vertical extension and the shape of the FOV weighting function is defined in distance (km). This results in a non-physical instrumental aperture dependent on tangent height, when the same weighting function is used for a total limb scan.
(b) Distortion of the FOV due to refraction is not taken into account.
KOPRA's concept is closer to the physical conditions: The FOV weighting function and its partitioning are defined in terms of elevation angle, which leads to a decrease (in distance) of the vertical extension of the FOV with increasing tangent height. Since refraction is also taken into account, the weighting function is additionally distorted.
We compare spectra convolved with the trapezoidal FOV weighting function originally defined by ESA, which is constant until ±1.4 km from nominal tangent height and decreases to zero at ±2 km (cf. Section 2.2). This function can be exactly modeled by the RFM. Due to consideration of refraction, the trapezoid is distorted within KOPRA. Moreover, for nominal instrumental aperture (half angle of 6.1×10^{-4} rad, assessed geometrically without consideration of refraction), KOPRA's FOV is vertically more extended at low tangent heights (e.g. ~4.3 km at 10 km) and less extended at higher altitudes. To obtain nearly consistent conditions for both codes, the FOV half angle of KOPRA was adjusted to 2 km for each tangent height, i.e. to 5.662×10^{-4} rad for 10 km. Further, we used a 12-point FOV representation for the RFM, which had been a good compromise between accuracy and computation time in the OFM-RFM intercomparison, and correspondingly represented the FOV of KOPRA by 11 or 13 point-radiance spectra (only odd numbers possible).
As expected, there is poor agreement for KOPRA calculations with the half angle of 6.1×10^{-4} rad (Figure 6b). The differences amount to 4 nW/(cm^2 sr cm^{-1}) at the line center and to 11 nW/(cm^2 sr cm^{-1}) at the line wings. KOPRA calculations with the RFM-adjusted half angle result in much better agreement. For 11 point-radiance spectra the difference is reduced to 0.1 nW/(cm^2 sr cm^{-1}) at line center and to 0.4 nW/(cm^2 sr cm^{-1}) at the line wings (Figure 6c). For 13 spectra the residuals at the line wings decrease further to -0.04 nW/(cm^2 sr cm^{-1}) (Figure 6d). This deviation is a factor of 3 more than for ALS convolved spectra, but still only

1% of NESR/4.

5.2 Isolated CO_2 Line, 40 km Tangent Height

The differences in the upper stratosphere are also very small. For unconvolved spectra and KOPRA calculations for an ellipsoidal Earth (Figure 7, top) the residuals are 0.05 nW/(cm^2 sr cm^{-1}) at the line center and -0.1 nW/(cm^2 sr cm^{-1}) at the line wings. KOPRA calculations for a spherical Earth remove the difference at the line center, but the deviation at the line wings remains. After convolution with the renormalized apodization function ils2001.nor (Figure 7, middle) the residuals decrease to -0.01 nW/(cm^2 sr cm^{-1}) at the line center and to 0.005 nW/(cm^2 sr cm^{-1}) at the line wings. FOV-convolution was performed with the trapezoidal weighting function in the same way as outlined in Section 5.1.3, but with a RFM-adjusted half-angle of 6.230×10^{-4} rad for KOPRA calculations. The differences at the line center is 0.02 nW/(cm^2 sr cm^{-1}), whereas the deviations at the line wings are smoothed out (Figure 7, bottom).

5.3 Full Microwindow Calculations

As a next step we performed spectral calculations for the same 6 MIPAS microwindows as in the OFM-RFM study:

(a) PT012A MW, 700.85-701.1 cm^{-1}, CO_2, 40 km,
(b) CH440A MW, 1355.0-1356.75 cm^{-1}, CH_4, 40 km,
(c) N2O20A MW, 1879.35-1880.3 cm^{-1}, N_2O, 10 km,
(d) O3014A MW, 763.5-764.65 cm^{-1}, O_3, 40 km,
(e) HNO08A MW, 888.5-891.2 cm^{-1}, HNO_3, 10 km,
(f) H2O17A MW, 1413.9-1416.4 cm^{-1}, H_2O, 10 km.

Beside the main target gas, the other 5 gases were also considered for each microwindow. Figures 8-13 show the spectra (a) and the differences for unconvolved (b), ALS convolved (c) and ALS and FOV convolved spectra (d) for each case.

5.3.1 Unconvolved Spectra

There is very good agreement between KOPRA and RFM spectra for the CH_4-, N_2O-, O_3-, HNO_3- and H_2O-microwindows (Figures 9b-13b). Due to the different Earth shapes assumed the maximum differences are generally at the line centers, but far below NESR/4. For O_3 they amount to -0.15 nW/(cm^2 sr cm^{-1}) and for CH_4 to 0.03 nW/(cm^2 sr cm^{-1}). These residuals could be further reduced by a factor of 4 by performing KOPRA calculations for a spherical Earth (cf. Section 5.1.1). The deviation of 0.2 nW/(cm^2 sr cm^{-1}) at the left edge of the H_2O-microwindow is caused by the line wing interpolation of the RFM (cf Section 4.2). The systematic offset of about -0.6 nW/(cm^2 sr cm^{-1}) in the CO_2-microwindow (Figure 8b) is not yet understood.

5.3.2 ALS and FOV Convolution

After convolution with the apodization function ils2001.nor the Doppler peaks in the line centers are smoothed out, which in most cases causes a reduction of the KOPRA-RFM residuals (Figures 8c-13c). However, the systematic offset in the p, T-microwindow is not removed (Figure 8c).

Finally the spectra were additionally convolved with the trapezoidal FOV weighting function in the same way as the isolated CO_2 line (Section 5.1.3). For the p, T- and O_3-microwindows the residuals are just as large as for ALS convolved spectra (Figures 8d, 11d). For CH_4 and N_2O they increase by one order of magnitude (Figures

9d, 10d), but are still far below NESR/4. Apart from two regions the agreement becomes only slightly worse for HNO_3 (Figure 12d). The most critical test of FOV calculations is the H_2O-microwindow (Figure 13d), because the H_2O profile has a strong change of gradient near the tangent height of 10 km. The resulting difference spectrum exhibits an offset of -0.1 nW/(cm^2 sr cm^{-1}) at the line wings and residuals of up to 0.35 nW/(cm^2 sr cm^{-1}) near the line centers. The reason of the offset is a slightly wider spacing of the point-radiance spectra calculated by KOPRA in the lower part of the FOV due to consideration of refraction.

The result of the full microwindow calculations is that for unconvolved, ALS convolved as well as for ALS and FOV convolved spectra the KOPRA-RFM differences fulfill the acceptance criteria, i.e. all residuals are well below NESR/4.

6 Special Physical Effects

6.1 CO_2 Line Mixing

Line mixing is the transfer of population between rotational-vibrational molecular states and redistribution of spectral intensity within a band, caused by collisions between the radiating molecule and a broadening gas. This effect is most significant at and near CO_2 Q-branches.

In the region of ± 10 cm^{-1} around the Q-branch head KOPRA models CO_2 line mixing following the approach of Strow et al. (Ref. [13, 14]). The user can either choose direct diagonalization of the relaxation matrix or the Rosenkranz first order approximation (Ref. [15]) and model either Q-branch- or QPR-branch-coupling. The RFM follows the same approach, but considers only Rosenkranz approximation and Q-branch-coupling. Further off the CO_2 Q-branch heads both codes parameterize line mixing and far wing effects by the so-called χ factors.

Test calculations for CO_2 line mixing were performed for limb paths with 10 km tangent height in the spectral region 787.5-797.5 cm^{-1}. This window contains the strong Q-branch at 791.6 cm^{-1}.

To show the magnitude of the effect, Figure 14 contains KOPRA calculations neglecting and including line-mixing (Rosenkranz approximation, Q-branch coupling). The largest difference of more than -600 nW/(cm^2 sr cm^{-1}) (for line mixing: lower values) appears at the left edge of the Q-branch ($\sim$791.2 cm^{-1}).

Figure 15a shows unapodized and ALS and FOV convolved KOPRA and RFM spectra with modeling of line mixing following the Rosenkranz approximation with Q-branch coupling. As a reference for the estimation of the residuals unapodized spectra calculated without line mixing are also presented. When line mixing is neglected, the residuals are very small with maximum differences of up to 0.5 nW/(cm^2 sr cm^{-1}) at the line centers and oscillations of about 0.1 nW/(cm^2 sr cm^{-1}) at the line wings (Figure 15b). As shown in Section 5, the former are mainly due to the different Earth shapes assumed and the latter due to the RFM's line wing interpolation. Inclusion of line mixing (Figures 15c,d) produces residuals very similar to the reference case. This shows that both codes model line mixing the same way. Again, the discontinuity of -0.4 nW/(cm^2 sr cm^{-1}) is probably caused by use of different Humlicek algorithms.

6.2 NLTE Calculations

In the lower and middle stratosphere most trace gases (except e.g. NO) are in local thermodynamic equilibrium (LTE), i.e. the populations of the lower and upper states of a vibrational-rotational transition are determined by the Boltzmann distribution evaluated at the local kinetic temperature. With increasing altitude collisional energy exchange is no longer sufficient to balance radiative or chemical pumping and the partition of populations is characterized by a temperature different from the local kinetic temperature, i.e. non-local thermodynamic equilibrium (NLTE) conditions develop.

In both codes, deviations from LTE are considered in the absorption cross-sections and in the source function. The RFM models NLTE emissions on the basis of externally supplied vibrational temperature profiles (Ref. [16, 17, 18]), whereas KOPRA can either use external population ratio or vibrational temperature profiles. The two codes handle layer-averaging of the NLTE parameter profiles slightly different. KOPRA calculates Curtis-Godson layer-averages of the vibrational temperatures or population ratios exactly the same way as for kinetic temperatures. The RFM, however, interpolates the vibrational-kinetic temperature difference profile to the Curtis-Godson pressure of the path segment and then adds it to the Curtis-Godson kinetic temperature.

NLTE calculations for CO_2 were performed using temperature and pressure profiles of the 1976 US Standard Atmosphere. The vibrational temperature profiles of CO_2, provided by the Instituto de Astrofisica de Andalucia (IAA), extended up to 120 km with 1 km vertical spacing (Ref. [19]). As a reference, Figure 16a shows unconvolved CO_2 spectra and KOPRA-RFM differences for 10 km tangent height and LTE conditions. The residuals are small ($<$0.4 nW/(cm^2 sr cm^{-1})) and similar to those of the isolated CO_2-line (cf. Figure 4a). Unapodized NLTE calculations on the 1 km vertical grid exhibit residuals between 0 and 20 nW/(cm^2 sr cm^{-1}) at the line centers and of 2 nW/(cm^2 sr cm^{-1}) at the inner line wings (Figure 16b). The large and irregular residuals at the line centers[2] are caused by different neglection of CO_2-signatures from the uppermost atmosphere. For an atmosphere ending at 80 km altitude the differences between the Doppler kernels are more regular and reduced to $\sim$-1.5 nW/(cm^2 sr cm^{-1}) (Figure 16c), whereas the residuals at the line wings remain the same. Much better agreement is achieved by using vertically highly resolved vibrational temperature profiles, consisting of 321 points with 250 m vertical spacing (Figure 16d). The residuals at the line wings nearly disappear, and the differences at the line centers of 1.2 nW/(cm^2 sr cm^{-1}) are just a factor of three larger than in the LTE-case. This indicates that the residuals for 1 km level-spacing are mainly due to the different averaging schemes of vibrational temperatures, which leads to larger deviations for wider layers.

Another set of NLTE calculations was performed for NO, using (a little unrealistic) *vmr*- and T_{vib}-profiles of the vibrational states 1, 11, 2 and 12 (HITRAN-notation) extending up to 200 km. Pressure and temperature profiles were taken from the MSIS90 model atmosphere for midlatitude March conditions. To investigate the effect of different layer-averaging of T_{vib}, the NLTE calculations were performed with 2.5 and 0.25 km vertical resolution, i.e. for 81 and 801 levels. Figure 17a shows unconvolved NO spectra and residuals for 10 km tangent height, 81 levels and LTE conditions. Like for CO_2, the residuals are very small ($<$0.004 nW/(cm^2 sr cm^{-1})). For NLTE calculations on the same vertical grid the KOPRA-RFM differences increase by a factor of 100 (Figure 17b). Again, the NLTE-residuals between the strong NO-lines at 1900.08 and at 1900.52 cm^{-1} decrease considerably, when the narrow vertical grid is applied (Figure 17c). The remaining difference at 1900.32 cm^{-1} results from transitions (13 -> 12 in HITRAN notation), for which no upper state vibrational temperature profiles were provided. In this case KOPRA calculates the LTE signature, whereas the RFM neglects the lines totally. When state 13 is formally represented by the vibrational temperatures and energy of state 12 in the input files, these lines also disappear in the KOPRA calculation and the artefact is removed (Figure 17d, only residuals plotted). Now it becomes obvious

---

[2] this effect does no longer appear for the KOPRA version of July 1999

that the NLTE-residuals are of the same magnitude as the LTE-residuals.

6.3 Continua

In addition to line-by-line absorption, continuum absorption must also be taken into account for strongly absorbing gases in atmospheric infrared spectroscopy. The largest continuum in the atmospheric windows around 4 μm and at 8-12 μm results from water vapor, for which both KOPRA and the RFM use the CKD.21 continuum model (Ref. [20]). They subtract the absorption coefficient evaluated at line center ± 25 cm^{-1} from each line and then add the continuum term. Differences can arise from lines being neglected due to their small contributions. The implementation of the H_2O continuum into the RFM code is discussed more in detail in Ref. [3]. In addition to H_2O, both codes enable calculation of a CO_2 continuum and of the pressure induced O_2 (Ref. [21] and N_2 absorption bands (Ref. [22]) at 1550 cm^{-1} and at 2350 cm^{-1}, respectively.

Figure 18 shows unapodized atmospheric limb spectra for 10 km tangent height. For H_2O the residua are very similar to the case without continuum (Figure 13b), which shows that also for limb paths both codes model the same continuum contribution. For O_2 and N_2 the KOPRA-RFM differences exhibit weak offsets of up to 0.015 and 0.004 nW/(cm^2 sr cm^{-1}), respectively. In addition there are weak residuals of up to 0.03 and -0.002 nW/(cm^2 sr cm^{-1}) at the line centers. All these deviations are far below NESR/4. (CO_2 continuum still to be validated)

6.4 Cross Section Spectra

To model the signature of heavy molecules as CFCs, $ClONO_2$, N_2O_5 and SF_6, for which in most cases line data are not available, both KOPRA and the RFM use laboratory measurements of absorption cross-sections. However, there are differences in data handling. The RFM was designed for HITRAN92 datasets, which are tabulated with equidistant temperature spacing and independently of pressure. Therefore this code interpolates linearly to atmospheric temperature, assuming equidistant T-spacing, but not to atmospheric pressure. Extrapolation beyond the tabulated temperature range is performed using the total internal partition sum. As far as available, KOPRA uses the most recent cross-section data, measured for various non-equidistant temperatures and pressures. Therefore it interpolates in temperature-pressure space, weighting the four (if available) nearest T,p-datasets in each of the quadrants adjacent to the observation by their reciprocal, normalized distance. T,p-extrapolation is performed similarly, using the tabulated data. The $ClONO_2$ cross-sections are interpolated reciprocally in temperature.

First we present $ClONO_2$ and N_2O_5 spectra, for which both codes use the same laboratory measurements of Ballard (Ref. [23]) and of Cantrell (Ref. [24]), respectively. Since these cross-sections are tabualated without specification of pressure, no differences result from KOPRA's pressure interpolation. The tabulated $ClONO_2$ dataset used by KOPRA was interpolated and extrapolated from the original measurements at 296 K and 213 K to 6 temperatures between 190 K and 296 K.

Figure 19 shows unapodized spectra of the ν_4 Q-branch of $ClONO_2$ for 10 km tangent height and a $ClONO_2$-profile measured by MIPAS-B on March 14, 1992 (Ref. [25]). First, the temperature profile of the 1976 US Standard Atmosphere was used. The uppermost KOPRA-RFM residual of Figure 19 exhibits a slightly negative offset at the wings and a positive deviation at the center of the Q-branch. Moreover there are various spikes of up to -40 nW/(cm^2 sr cm^{-1}), due to different wavenumber grids. Whereas the RFM maintained the fine grid, KOPRA changed to 0.008 cm^{-1} spacing. RFM calculations on the same grid remove the spikes (Figure 19, middle). The remaining residuals of -2 nW/(cm^2 sr cm^{-1}) at the wings and of 8 nW/(cm^2 sr cm^{-1}) at the center of the Q-branch are due to different temperature extrapolation to the minimum of the temperature profile (216.7 K) as well as to different interpolation. However, spectra calculated for one of the temperature values (296 K), at which the cross-sections were measured, exhibit differences below 1.5 nW/(cm^2 sr cm^{-1}). In this case both codes do not interpolate and the agreement becomes as good as for line data gases.

Figure 20 shows unapodized atmospheric limb spectra of the ν_{12} band of N_2O_5 for 10 km tangent height. For the 1976 US Standard temperature profile the KOPRA-radiances are systematically below the RFM-values by about -12%, which means poor agreement (top). This is due to different temperature extrapolation from the "coldest" cross-section dataset (233 K) to the minimum of the temperature profile (216.7 K). For a constant temperature profile of 273 K, which is the temperature of one of the tabulated datasets, the residuals decrease to ±0.04 nW/(cm^2 sr cm^{-1}) or ±0.5% (bottom).

To model CFC-12 (CCl_2F_2) spectra, KOPRA takes cross-sections of Varanasi (Ref. [26]), which are given for various non-equidistant atmospheric temperatures and pressures. The RFM originally used another dataset, which is tabulated without specification of pressure (Ref. [27]). For the intercomparison the Varanasi dataset from the HITRAN96 database, consisting of 15 non-equidistant p, T-points, was supplied for both codes. Due to the non-appropriate interpolation scheme of the RFM, Figure 21 (top) exhibits residuals of up to 30 nW/(cm^2 sr cm^{-1}) even for homogeneous path conditions of 250 km, 250 hPa and 220 K. To avoid interpolation, homogeneous KOPRA and RFM calculations were performed for the tabulated values of 296.2 K and 790.5 Torr (1054 hPa) with 0.008 cm^{-1} resolution. Again, for this p, T-value the differences become smaller than 0.5 nW/(cm^2 sr cm^{-1}) (Figure 21, bottom).

6.4.1 Spectral Derivatives

Additionally to the calculation of the spectrum, KOPRA is able to determine the derivatives of the spectrum with respect to most of the retrieval parameters, e.g. to kinetic and vibrational temperature, volume mixing-ratio, horizontal gradients of temperature and volume mixing-ratio. These derivatives are determined analytically during one forward calculation. Thus time-consuming numerical derivatives, i.e. variation of each parameter and recalculation of the disturbed spectrum, become unnecessary. However to optimize run-time, some simplifications are made. A detailed description of the method is given by Ref. [28]. In this Section we compare analytical with numerical derivatives calculated by KOPRA (cf. Ref. [28]).

Figure 22 shows derivatives of a HNO_3-spectrum with respect to volume-mixing-ratio and to temperature at tangent height (20 km). The *vmr* derivatives differ by less than ±2%, which means very good agreement. The T derivatives exhibit an offset of about -8% and a larger scatter. However, in real retrievals T derivatives of HNO_3 will only be necessary for error estimation. The T derivatives of CO_2 are more important, since this trace gas will be used for p, T-retrievals. Figure 23 shows the derivatives at 10 km and 40 km tangent height. The deviations are more smoothly and smaller, -6% and 4% at the wavenumber regions with highest temperature sensitivity. Figure 24 contains the *vmr* derivatives of a H_2O line at 10 km tangent height. Due to saturation a wide region around line center is no longer sensitive on *vmr* variations (cf. Figure 23, top). The deviations at the maxima of the derivatives are about 6%.

7 Conclusions

The KOPRA-RFM intercomparison shows, that there are no significant differences in ray-tracing, integrated column amounts and Curtis-Godson parameters. The difference spectra are significantly less than NESR/4 for the isolated CO_2 line as well as for six MIPAS microwindows and thus KOPRA fulfills the acceptance criteria. In most cases the deviations are even clearly below 1 nW/(cm^2 sr cm^{-1}), i.e. more than one order of magnitude below the acceptance threshold. This is generally valid for unconvolved as well as for ALS and FOV convolved spectra. There is also good agreement in modeling of the H_2O-, O_2- and N_2-continua and of CO_2 line-mixing. Somewhat larger deviations of several nW/(cm^2 sr cm^{-1}) were found for NLTE calculations with "default" vertical resolution (1 km or 2.5 km), caused by different layer-averaging of the vibrational temperatures. The differences could be considerably reduced by using profiles of higher vertical resolution of 250 m. Cross-section spectra agree well, if the tabulated data are given without specification of pressure, e.g. for $ClONO_2$ and N_2O_5, and cover the atmospheric temperatures. Due to different temperature extrapolation the deviations increase up to 10 nW/(cm^2 sr cm^{-1}) for atmospheric temperatures outside the tabulated range. The RFM is not yet adjusted to cross-sections given for non-equidistant temperature and pressure values, like CFC data in the HITRAN96 database. Thus there are differences of 30 nW/(cm^2 sr cm^{-1}) for e.g. CFC-12 for typical stratospheric conditions. However, the deviations decrease below 0.5 nW/(cm^2 sr cm^{-1}) for homogeneous path calculations using p, T of a tabulated dataset. There is sufficiently good agreement between analytical and numerical derivatives.

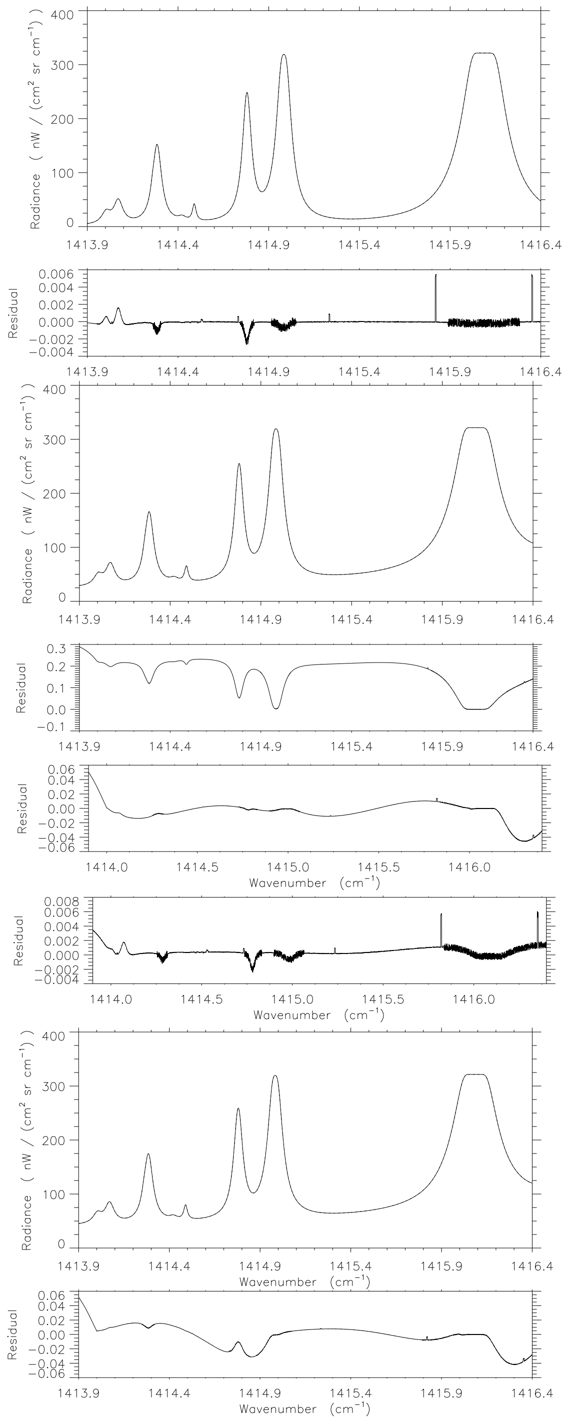

Figure 3: Unapodized H_2O radiance spectra and KOPRA-RFM differences for a homogeneous path (250 hPa, 220 K) and KOPRA accuracy of 10^{-10}. (a) Only lines inside the microwindow considered, (b) additionally lines within $\pm 32\text{cm}^{-1}$ (KOPRA) and $\pm 25\text{cm}^{-1}$ (RFM) from the microwindow's edges considered, (c) for both codes lines within ± 25 cm^{-1} considered, (d) same as (c) but RFM's fine-mesh extended to ± 5 cm^{-1}, (e) same as (c) but additionally H_2O continuum considered.

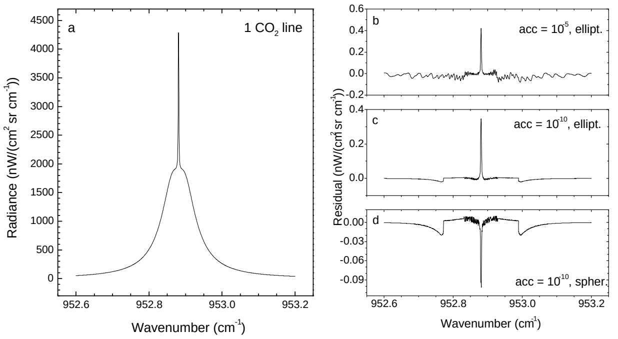

Figure 4: (a) Isolated CO_2 line, unapodized, 10 km tangent height; residuals for KOPRA calculations for ellipsoidal Earth and an accuracy of (b) 10^{-5} and (c) of 10^{-10}, (d) for KOPRA calculations for spherical Earth and an accuracy of 10^{-10}.

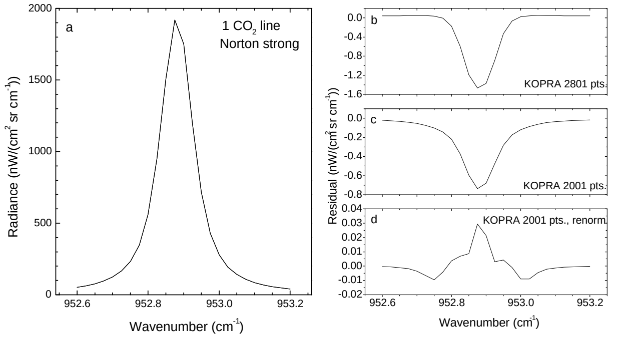

Figure 5: (a) Isolated CO_2 line, convolved with Norton-Beer strong function, 10 km tangent height; residuals for (b) different spectral extensions of the apodization functions (RFM 2001, KOPRA 2801 spectral points), (c) both functions with 2001 points, (d) KOPRA's apodization function additionally renormalized as by the RFM.

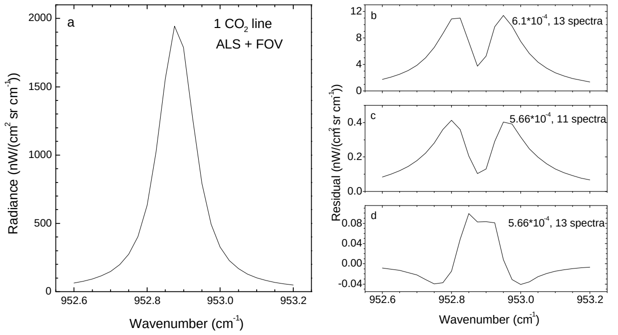

Figure 6: (a) Isolated CO_2 line, ALS and FOV convolved, 10 km tangent height; RFM calculations with 12 point-radiance spectra. Residuals for KOPRA calculations for nominal FOV half-angle of 6.1×10^{-4} rad and 13 spectra (b), for RFM-adjusted half-angle of FOV extension and 11 spectra (c), for RFM-adjusted half-angle of FOV extension and 13 spectra (d).

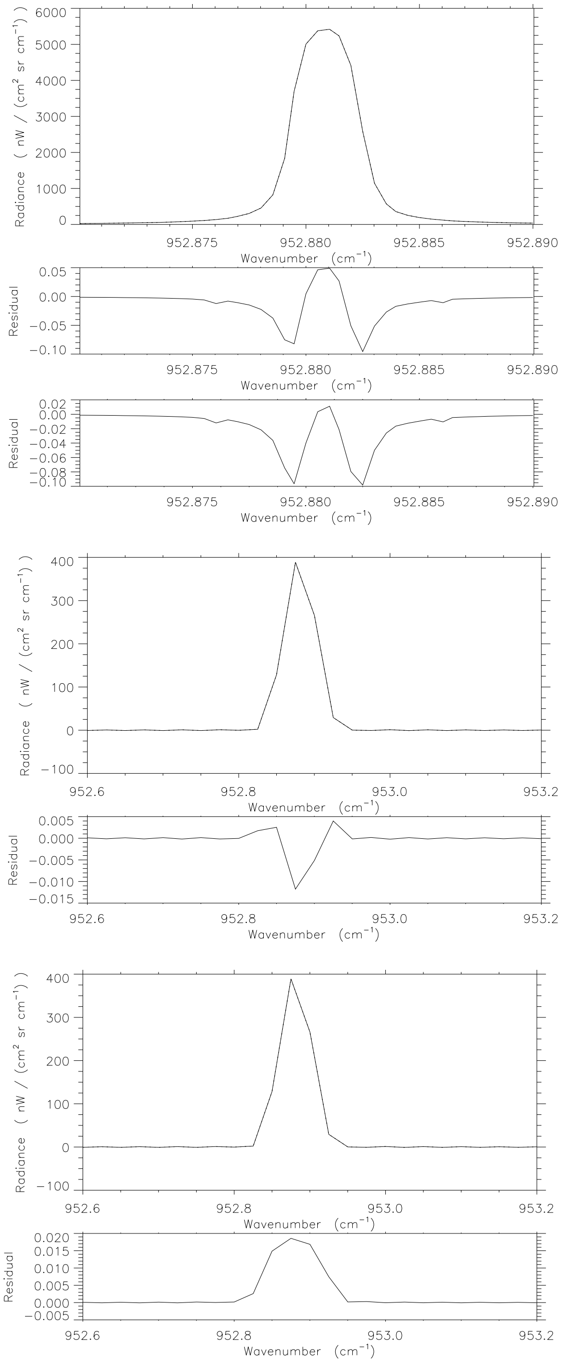

Figure 7: Isolated CO_2 line, 40 km tangent height, KOPRA's accuracy 10^{-10}; top: unconvolved spectrum, differences for KOPRA calculations for ellipsoidal Earth and spherical Earth; middle: ALS convolution (ils2001.nor); bottom: ALS and FOV convolution, FOV-modeling with 12 (RFM) and 13 (KOPRA) point-radiance spectra, KOPRA's FOV RFM-adjusted.

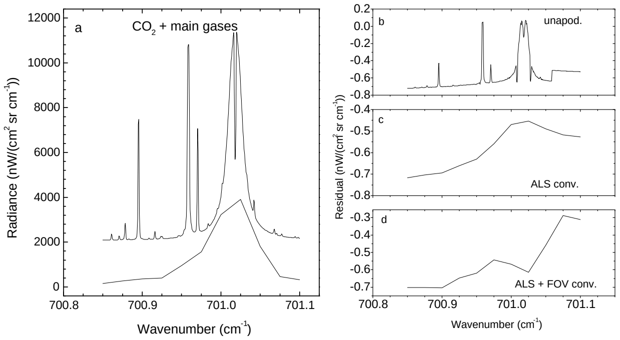

Figure 8: (a) p, T-microwindow, 40 km tangent height, unapodized (offset 2000 nW/(cm^2 sr cm^{-1})) and ALS+FOV convolved spectra; residuals for (b) unapodized spectra, (c) ALS convolved spectra, (d) ALS and FOV convolved spectra, KOPRA calculations for RFM-adjusted FOV extension.

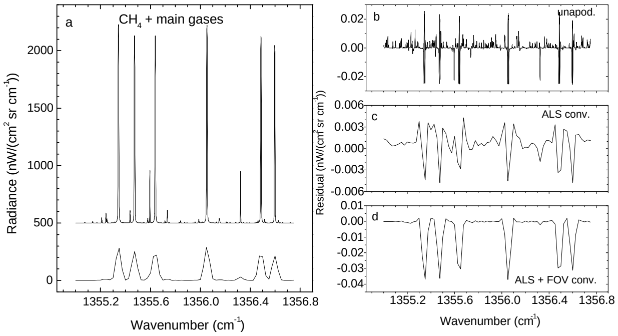

Figure 9: Same as Figure 8, but for a CH$_4$-microwindow, 40 km tangent height, unapodized spectra shifted by 500 nW/(cm^2 sr cm^{-1}).

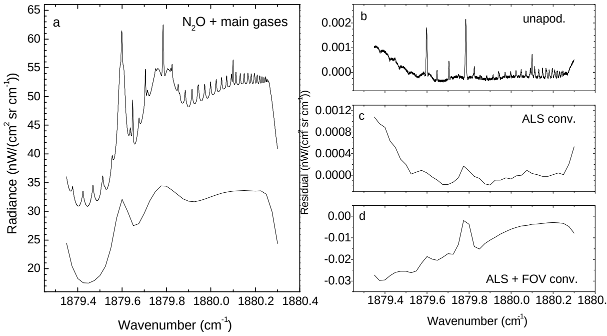

Figure 10: Same as Figure 8, but for a N$_2$O-microwindow, 10 km tangent height, unapodized spectra shifted by 20 nW/(cm^2 sr cm^{-1}).

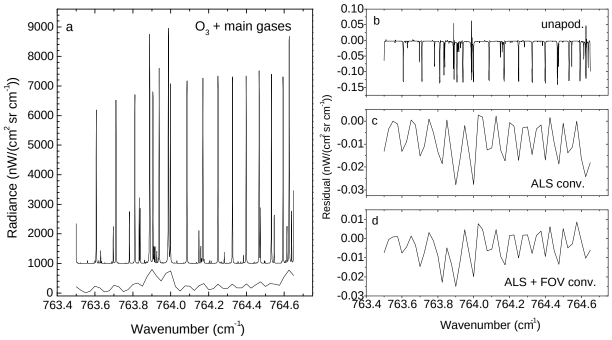

Figure 11: Same as Figure 8, but for an O_3-microwindow, 40 km tangent height, unapodized spectra shifted by 1000 nW/(cm^2 sr cm^{-1}).

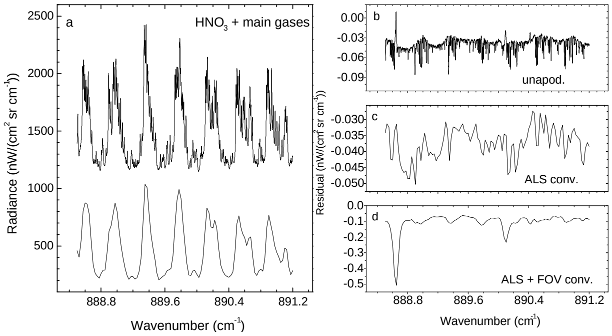

Figure 12: Same as Figure 8, but for a HNO_3-microwindow, 10 km tangent height, unapodized spectra shifted by 1000 nW/(cm^2 sr cm^{-1}).

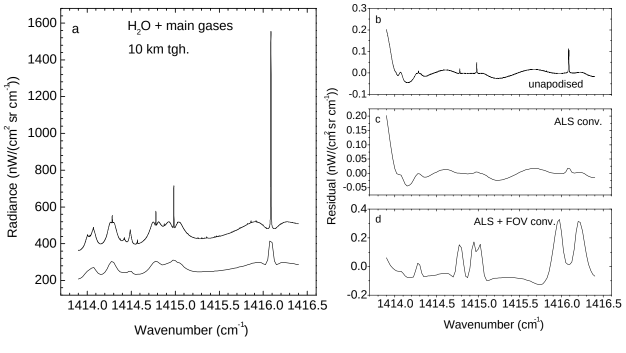

Figure 13: Same as Figure 8, but for a H_2O-microwindow, 10 km tangent height, unapodized spectra shifted by 200 nW/(cm^2 sr cm^{-1}).

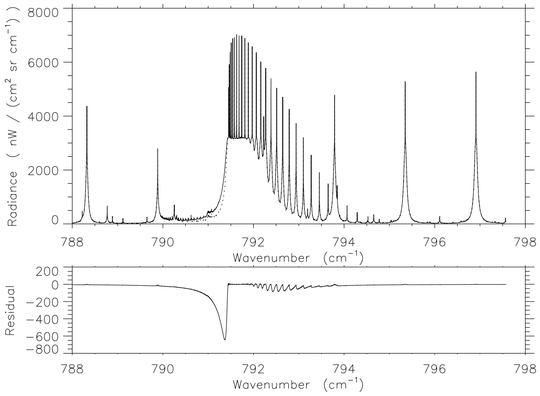

Figure 14: Unapodized KOPRA spectra containing the CO_2-Q-branch at 791.6 cm^{-1}, 10 km tangent height; differences between KOPRA calculations neglecting line-mixing and including line-mixing (Rosenkranz approximation and Q-branch coupling).

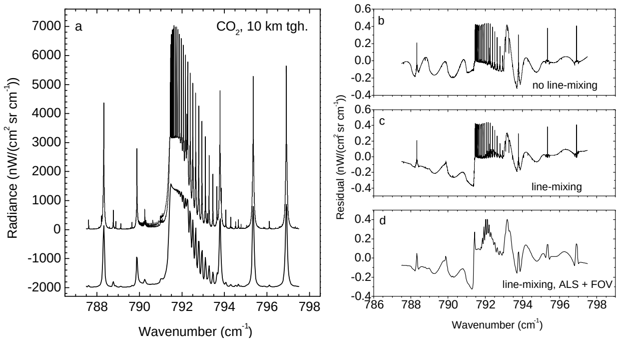

Figure 15: (a) CO_2-microwindow containing the Q-branch at 791.6 cm^{-1}, unapodized and ALS+FOV convolved spectra (shifted by -2000nW/(cm^2 sr cm^{-1}). Residuals for (b) unapodized spectra, no line-mixing, (c) unapodized spectra, line-mixing with Rosenkranz approximation, (d) ALS and FOV convolved spectra, line-mixing with Rosenkranz approximation.

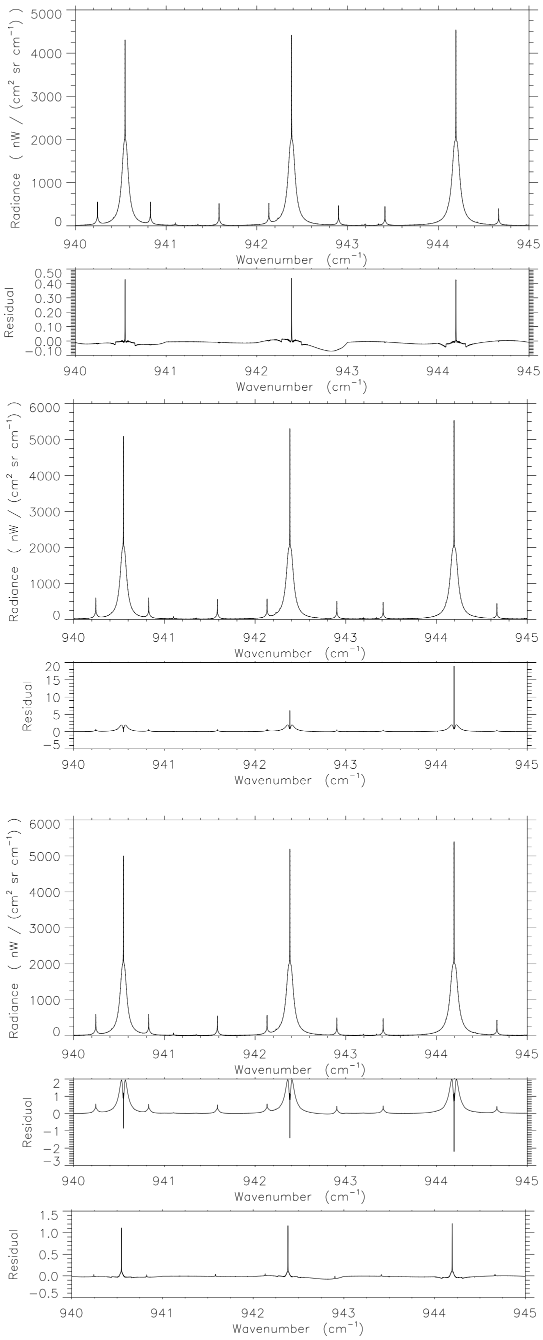

Figure 16: CO_2-microwindow, 10 km tangent height, unapodized spectra and residuals for (a) LTE-conditions (as reference) and atmospheric profiles with 1 km vertical resolution up to 120 km, (b) NLTE-calculations for 1 km spacing up to 120 km (also T_{vib}), (c) NLTE-calculations for 1 km spacing up to 80 km and (d) NLTE-calculations for 250 m spacing up to 80 km (only residuals shown).

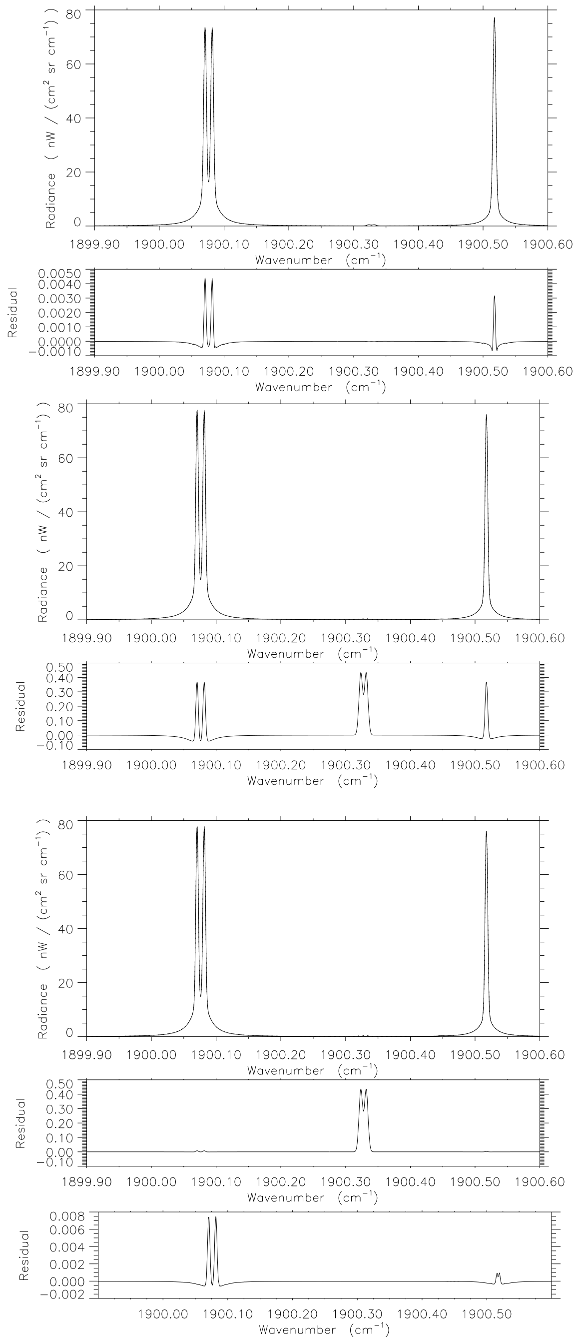

Figure 17: NO-microwindow, 10 km tangent height, unapodized spectra and residuals for (a) LTE-conditions and atmospheric profiles with 2.5 km spacing up to 200 km (as reference), (b) NLTE-calculations for 2.5 km spacing up to 200 km (also T_{vib}), (c) NLTE-calculations for 250 m spacing up to 200 km and (d) same as in (c), but lines at 1900.32 cm^{-1} also taken into account by RFM (only residual shown).

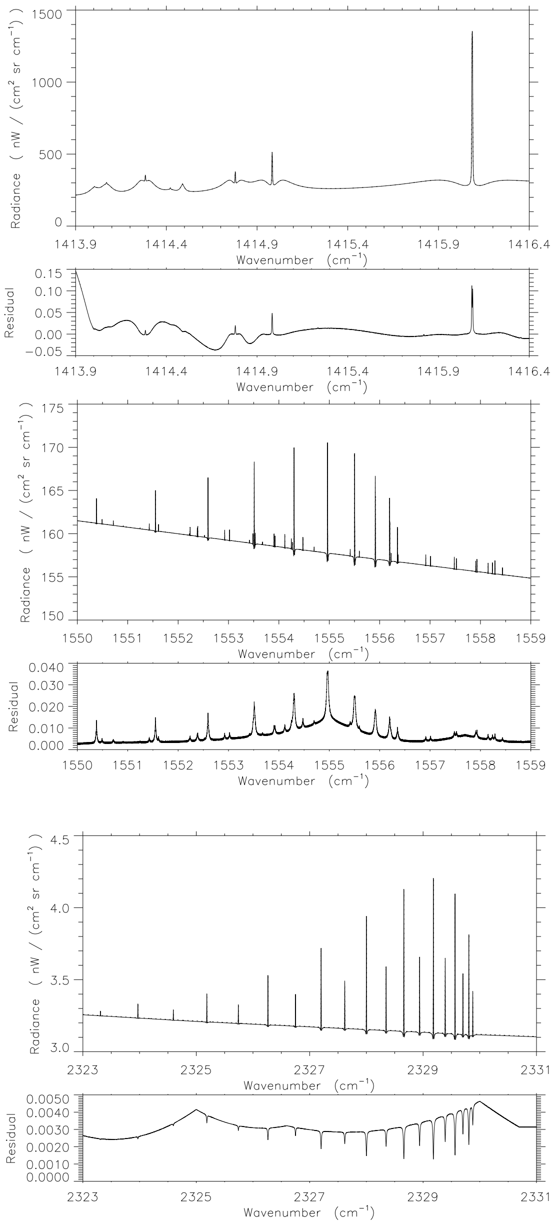

Figure 18: Unapodized spectra for 10 km tangent height, top: H_2O-microwindow including the H_2O-continuum, middle: O_2-microwindow with O_2-continuum, bottom: N_2-microwindow with N_2-continuum.

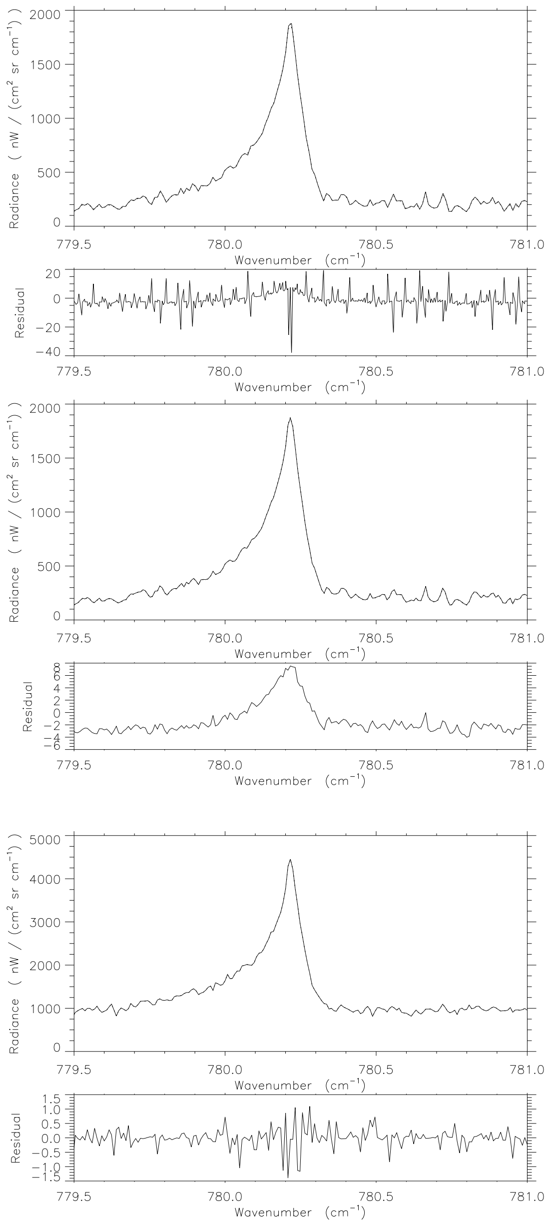

Figure 19: Unapodized $ClONO_2$ cross-section spectra for 10 km tangent height and KOPRA-RFM deviations. Top: different wavenumber grids (KOPRA 0.008 cm^{-1}, RFM 0.0005 cm^{-1}), middle: both codes same wavenumber grids (0.008 cm^{-1}), bottom: both codes same wavenumber grids and isothermal atmosphere (296 K).

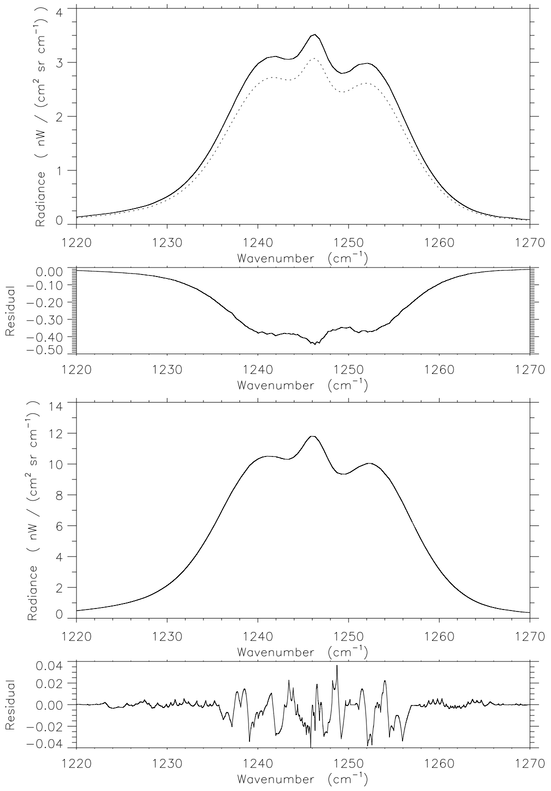

Figure 20: Unapodized N_2O_5 cross-section spectra for 10 km tangent height and KOPRA-RFM deviations for (top) 1976 US Standard Atmosphere and (bottom) isothermal atmosphere (273 K).

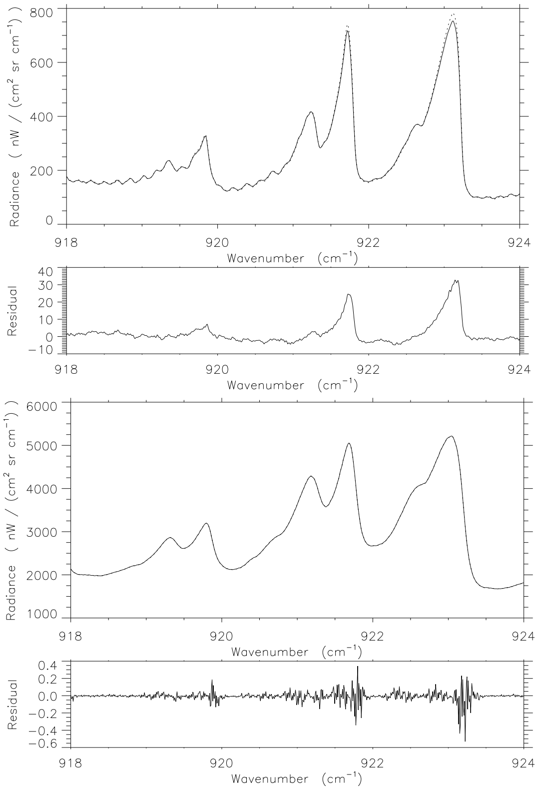

Figure 21: Unapodized CFC-12 (CCl_2F_2) cross-section spectra for homogeneous path conditions (250 km). Top: KOPRA and RFM calculations for 250 hPa and 220 K, bottom: calculations for 1054 hPa and 296.2 K.

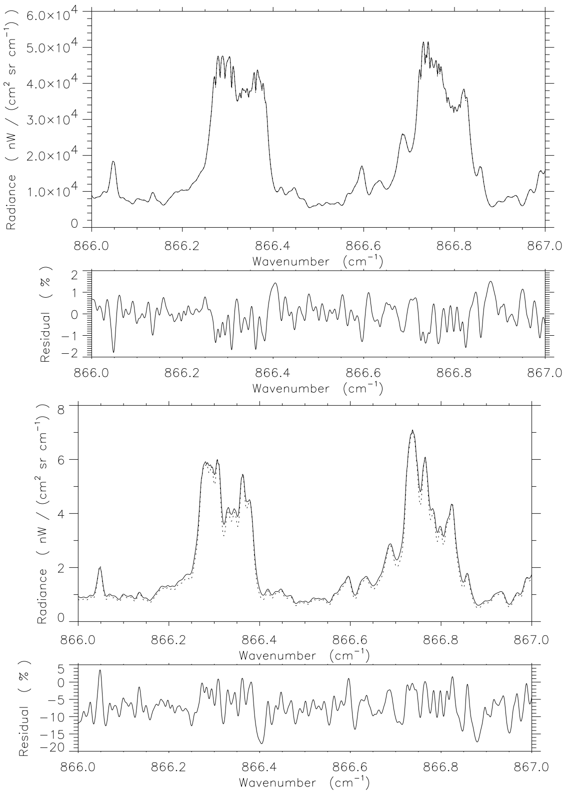

Figure 22: Analytical and numerical derivatives of an unapodized HNO_3-spectrum with respect to volume-mixing ratio (top) and temperature (bottom) at tangent height (20 km) and differences (numerical - analytical).

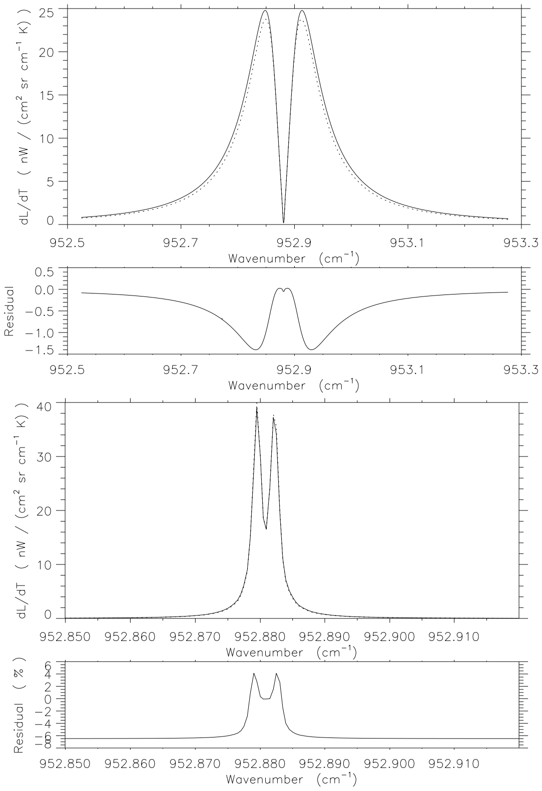

Figure 23: Analytical and numerical derivatives of unapodized CO_2-spectra with respect to temperature at tangent height of 10 km (top) and 40 km (bottom) and differences (numerical - analytical).

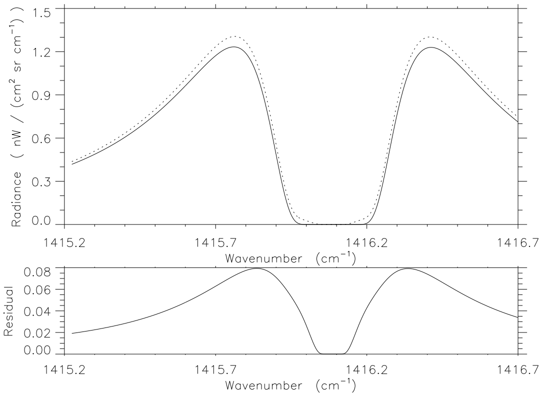

Figure 24: Analytical and numerical derivative of an unapodized H_2O-spectrum with respect to volume-mixing ratio at tangent height (10 km) and differences (numerical - analytical).

Appendix A

RFM- and KOPRA-Modifications to minimize CO_2-Residuals

In Figure 25 we show unapodized CO_2-lines for 10 km tangent height and summarize the reductions of KOPRA-RFM residuals, which can be obtained by slight modifications of the two codes. The first residual spectrum results from calculations using the standard versions of the codes and contains several spikes, oscillations and discontinuities. Although these features are very small compared to NESR/4 (12.5 nW/(cm^2 sr cm^{-1})), we tried to find the reason of the differences. The oscillations at e.g. 940.8 and 942.8 cm^{-1} are due to the wide-mesh interpolation of the RFM and can be removed by extending the RFM's fine-mesh area to ± 5 cm^{-1} (second residual spectrum). The spikes are for the most part caused by the different Earth shapes assumed (KOPRA: ellipsoidal Earth, RFM: spherical Earth) and are reduced from 0.35 to -0.1 nW/(cm^2 sr cm^{-1}) by a modified KOPRA version calculating with a spherical Earth shape (third residual). The discontinuities close to the spikes result from different Humlicek-algorithm realizations. Whereas KOPRA uses a fast version for calculations including χ-factor, the RFM takes the standard version. For simulations without χ-factor the RFM also applies the fast version and the discontinuities nearly disappear (fourth residual). The remaining small positive spikes are due to slightly different extensions of the evaluation regions of the fast Humlicek-algorithm.

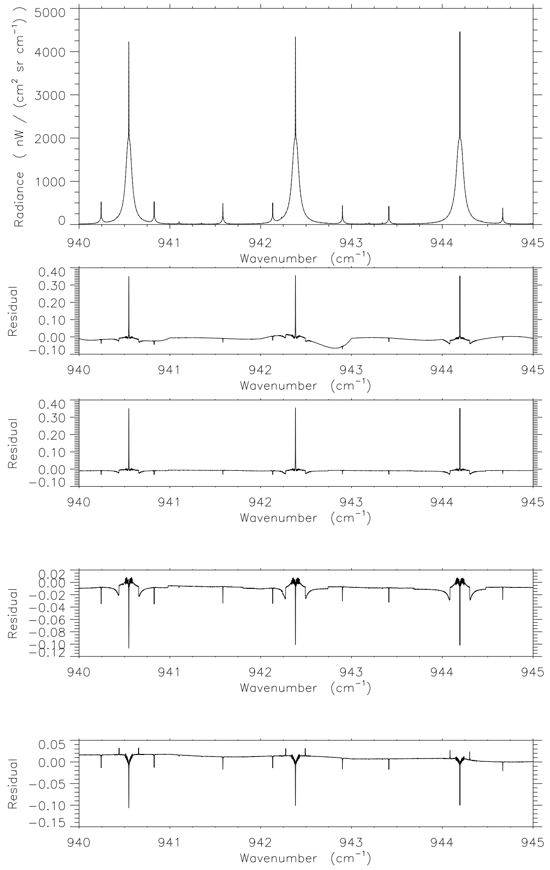

Figure 25: Unapodized CO_2-spectra, 10 km tangent height. Residuals for calculations (a) with χ-factor, standard program versions, (b) with χ-factor, RFM's fine-mesh extended to ±5 cm^{-1}, (c) with χ-factor, RFM's fine-mesh extended to ±5 cm^{-1}, KOPRA calculations for spherical Earth, (d) same as (c), but without χ-factor.

Appendix B

FOV-Modeling by KOPRA

Figure 26 contains ALS and FOV convolved H_2O-spectra calculated by KOPRA for 10 km tangent height. The residuals result from FOV-modeling by different numbers of point-radiance spectra. The upper plot contains the reference spectrum modeled by 39 and a spectrum modeled by just 3 point-radiance spectra. The respective difference spectrum (second plot) exhibits systematic deviations of up to -8 nW/(cm^2 sr cm^{-1}) at the line wings. The additional plots show the deviations between the reference case and spectra modeled by 9, 13 and 30 point-radiance spectra. The residuals successively decrease to 0.02 nW/(cm^2 sr cm^{-1}) in the lowermost plot. For FOV-modeling by 13 spectra, as performed in the KOPRA-RFM intercomparison, the differences amount to ±0.4 nW/(cm^2 sr cm^{-1}).

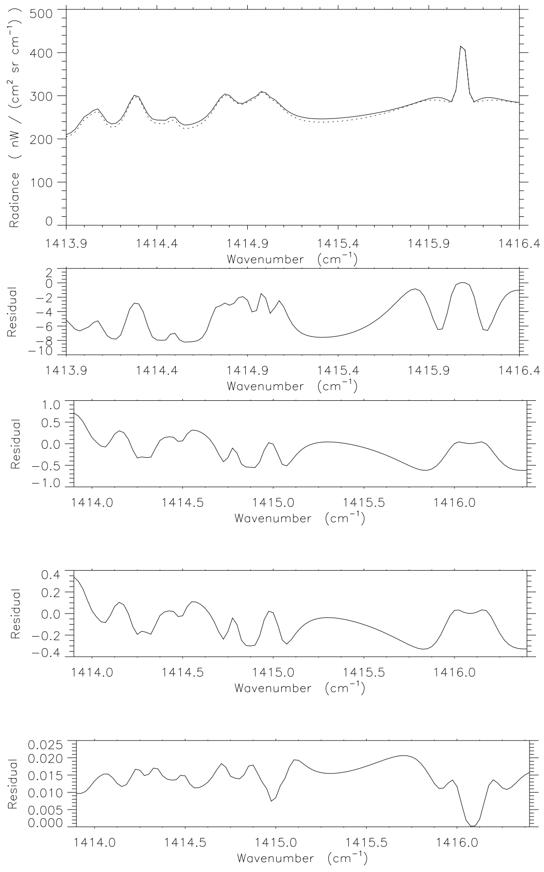

Figure 26: ALS and FOV convolved H_2O-spectra calculated by KOPRA for 10 km tangent height. A reference spectrum (—) was created using 39 point-radiance spectra. The second spectrum (···) and the first residual result from FOV-modeling by 3, the additional residuals from FOV-modeling by 9, 13 and 30 point-radiance spectra.

Bibliography

[1] A. Dudhia and P. Raspollini, "Results of intercomparisons of the OFM and the RFM code PO-TN-OXF-GS-0007," tech. rep., Oxford University and IROE, December, 9, 1996. Combination of Task Reports on Task 2.1 (PO-SW-ESA-GS-0315) and Task 3.3 (PO-SW-ESA-GS-00323) of ESA Contract 12055/96/NL/CN.

[2] G. P. Stiller, M. Höpfner, M. Kuntz, T. von Clarmann, G. Echle, H. Fischer, B. Funke, N. Glatthor, F. Hase, and S. Zorn, "The Karlsruhe Optimized and Precise Radiative transfer Algorithm (KOPRA): Realization, model error assessment and a posteriori justification," in *Proc. European Symposium on Atmospheric Measurements from Space, ESAMS'99, 18–22 Jan 1999, Noordwijk*, pp. 749–756, European Space Agency, ESTEC, Noordwijk, The Netherlands, 1999.

[3] P. Morris, A. Darbyshire, and A. Dudhia, "MIPAS–development of a reference forward algorithm for the simulation of MIPAS atmospheric limb emission spectra – detailed design document," tech. rep., European Space Agency, 1997. Report of ESA Contract 11886/96/NL/GS.

[4] N. Glatthor, M. Höpfner, G. P. Stiller, T. von Clarmann, A. Dudhia, G. Echle, B. Funke, and F. Hase, "Intercomparison of the KOPRA and the RFM radiative transfer codes," in *Proc. European Symposium on Atmospheric Measurements from Space, ESAMS'99, 18–22 Jan 1999, Noordwijk*, pp. 757–764, European Space Agency, ESTEC, Noordwijk, The Netherlands, 1999.

[5] G. Echle, H. Oelhaf, and A. Wegner, "Measurement of atmospheric parameters with MIPAS," tech. rep., European Space Agency, December 1992. Final Report of ESA Contract 9597/91/NL/SF.

[6] L. S. Rothman, C. P. Rinsland, A. Goldman, T. Massie, D. P. Edwards, J.-M. Flaud, A. Perrin, C. Camy-Peyret, V. Dana, J.-Y. Mandin, J. Schroeder, A. McCann, R. R. Gamache, R. B. Wattson, K. Yoshino, K. V. Chance, K. W. Jucks, L. R. Brown, V. Nemtchinov, and P. Varanasi, "The HITRAN molecular spectroscopic database and HAWKS (HITRAN atmospheric workstation): 1996 edition," *J. Quant. Spectrosc. Radiat. Transfer* **60**(5), pp. 665–710, 1998.

[7] H. Norton and R. Beer, "New apodizing functions for Fourier spectrometry," *J. Opt. Soc. Am* **66**(3), pp. 259–264, 1976. (Errata J. Opt. Soc. Am., 67, 419,1977).

[8] F. Hase and M. Höpfner, "Atmospheric ray path modeling for radiative transfer algorithms," *Appl. Opt.* **38**(15), pp. 3129–3133, 1999.

[9] J. Humlicek, "Optimized computation of the Voigt and complex probability functions," *J. Quant. Spectrosc. Radiat. Transfer* **27**(4), pp. 437–444, 1982.

[10] M. Kuntz, "A new implementation of the Humlicek algorithm for the calculation of the Voigt profile function," *J. Quant. Spectrosc. Radiat. Transfer* **57**(6), pp. 819–824, 1997.

[11] R. J. Wells, "Rapid approximation to the Voigt/Faddeeva function and its derivatives," *J. Quant. Spectrosc. Radiat. Transfer* **62**(1), pp. 29–48, 1999.

[12] M. Kuntz and M. Höpfner, "Efficient line–by–line calculation of absorption coefficients," *J. Quant. Spectrosc. Radiat. Transfer* **63**(1), pp. 97–114, 1999.

[13] L. L. Strow and D. Reuter, "Effect of line mixing on atmospheric brightness temperatures near 15 μm," *Appl. Opt.* **27**(5), pp. 872–878, 1988.

[14] L. L. Strow, D. C. Tobin, and S. E. Hannon, "A compilation of first–order line–mixing coefficients for CO_2 Q–branches," *J. Quant. Spectrosc. Radiat. Transfer* **52**(3/4), pp. 281–294, 1994.

[15] P. W. Rosenkranz, "Shape of the 5 mm oxygen band in the atmosphere," *IEEE Transactions on Antennas and Propagation* **AP–23**(4), pp. 498–506, 1975.

[16] D. P. Edwards, M. López-Puertas, and M. Á. López-Valverde, "Non–local thermodynamic equilibrium studies of the 15 μm bands of CO_2 for atmospheric remote sensing," *J. Geophys. Res.* **98**(D8), pp. 14,955–14,977, 1993.

[17] D. P. Edwards, M. López-Puertas, and M. G. Mlynczak, "Non–local thermodynamic equilibrium limb radiance from O_3 and CO_2 in the 9–11 μm spectral region," *J. Quant. Spectrosc. Radiat. Transfer* **52**(3–4), pp. 389–407, 1994.

[18] D. P. Edwards, M. López-Puertas, and R. R. Gamache, "The non–LTE correction to the vibrational component of the internal partition sum for atmospheric calculation," *J. Quant. Spectrosc. Radiat. Transfer* **59**(3–5), pp. 423–436, 1998.

[19] M. López-Puertas, G. Zaragoza, M. Á. López-Valverde, F. J. Martín-Torres, G. M. Shved, R. O. Manuilowa, A. A. Kutepov, O. Gusev, T. von Clarmann, A. Linden, G. Stiller, A. Wegner, H. Oelhaf, D. P. Edwards, and J.-M. Flaud, "Non–local thermodynamic equilibrium limb radiances for the MIPAS instrument on ENVISAT–1," *J. Quant. Spectrosc. Radiat. Transfer* **59**(3–5), pp. 377–403, 1998.

[20] S. A. Clough, F. X. Kneizys, and R. W. Davies, "Line shape and the water vapor continuum," *Atmospheric Research* **23**, pp. 229–241, 1989.

[21] F. Thibault, V. Menoux, R. Le Doucen, L. Rosenmann, J.-M. Hartmann, and C. Boulet, "Infrared collision–induced absorption by O_2 near 6.4 μm for atmospheric applications: measurements and empirical modeling," *Appl. Opt.* **36**(3), pp. 563–567, 1997.

[22] W. J. Lafferty, A. M. Solodov, A. Weber, W. B. Olson, and J.-M. Hartmann, "Infrared collision–induced absorption by N_2 near 4.3 μm for atmospheric applications: measurements and empirical modeling," *Appl. Opt.* **35**(30), pp. 5911–5917, 1996.

[23] J. Ballard, W. B. Johnston, M. R. Gunson, and P. T. Wassell, "Absolute absorption coefficients of $ClONO_2$ infrared bands at stratospheric temperatures," *J. Geophys. Res.* **93**(D2), pp. 1659–1665, 1988.

[24] C. A. Cantrell, J. A. Davidson, A. H. McDaniel, R. E. Shetter, and J. G. Calvert, "Infrared absorption cross sections for N_2O_5," *Chem. Phys. Lett.* **148**, pp. 358–363, 1988.

[25] T. von Clarmann, H. Fischer, F. Friedl-Vallon, A. Linden, H. Oelhaf, C. Piesch, M. Seefeldner, and W. Völker, “Retrieval of stratospheric O_3, HNO_3 and $ClONO_2$ profiles from 1992 MIPAS–B limb emission spectra: Method, results and error analysis,” *J. Geophys. Res.* **98**(D11), pp. 20,495–20,506, 1993.

[26] P. Varanasi and V. Nemtchinov, “Thermal infrared absorption coefficients of CFC–12 at atmospheric conditions,” *J. Quant. Spectrosc. Radiat. Transfer* **51**(5), pp. 679–687, 1994.

[27] S. T. Massie, A. Goldman, A. H. McDaniel, C. A. Cantrell, J. A. Davidson, R. E. Shetter, and J. G. Calvert, “Temperature dependent infrared cross sections for CFC–11, CFC–12, CFC–13, CFC–14, CFC–22, CFC–113, CFC–114, and CFC–115,” tech. rep., NCAR, 1991. Technical Note, TN–358+STR.

[28] M. Höpfner, G. P. Stiller, M. Kuntz, T. von Clarmann, G. Echle, B. Funke, N. Glatthor, F. Hase, H. Kemnitzer, and S. Zorn, “The Karlsruhe optimized and precise radiative transfer algorithm. Part II: Interface to retrieval applications,” in *Optical Remote Sensing of the Atmosphere and Clouds, Beijing, China, 15–17 September 1998*, J. Wang, B. Wu, T. Ogawa, and Z. Guan, eds., *Proc. SPIE* **3501**, pp. 186–195, 1998.